Journal of Fluids and Structures 83 (2018) 471–489

Contents lists available at ScienceDirect

Journal of Fluids and Structures

journal homepage: www.elsevier.com/locate/jfs

The effect of bogies on high-speed train slipstream and wake

Shibo Wang [a,*], David Burton [a], Astrid Herbst [b], John Sheridan [a], Mark C. Thompson [a]

[a] Fluids Laboratory for Aeronautical and Industrial Research (FLAIR), Department of Mechanical Engineering, Monash University, Australia

[b] Centre of Competence for Aero- and Thermodynamics, Bombardier Transportation, Västeras, Sweden

ARTICLE INFO

Article history:
Received 3 November 2017
Received in revised form 14 February 2018
Accepted 26 March 2018

Keywords:
High-speed train
Train aerodynamics
Bogies
Slipstream
Wake structures
Computational fluid dynamics (CFD)
Detached eddy simulation (DES)

ABSTRACT

Slipstream, which is the induced air movement generated by a high-speed train (HST) as it passes, is both a safety hazard to commuters and trackside workers, and can cause damage to infrastructure along track lines. Bogies have been shown to exert a strong influence on HST aerodynamics by altering the underbody flow, and their effects have been extensively studied previously from the perspectives of ballast flight and drag reduction. In contrast, the effect of bogies on slipstream characteristics, and especially on the structure of the wake, is less well understood. This study explicitly investigates the effect of bogies on HST slipstream characteristics based on two generic train configurations: a *Simplified Train Model* (M1) with the bogies covered by a flat surface, and a *Full-featured Train Model* (M2) with simplified bogie-sets. The bogie effects are revealed through a systematic comparison of flow structures, slipstream characteristics and aerodynamic forces between these configurations. Remarkably, this study discovers that the generation of the strong spanwise oscillation of the wake, observed especially in the presence of bogies, can be interpreted as due to seeding and amplification of a natural instability of the time-mean pair of counter-rotating vortices behind the tail, rather than through direct side-to-side vortex shedding from the bogie geometry. This paper also documents how the altered wake flow affects slipstream characteristics through statistical and gust analyses, and the effect of the bogies on aerodynamic loading by comparing the train surface pressure distributions between the configurations.

1. Introduction

High-speed trains (HSTs) have proven to be a viable intercity transportation method because of their high transportation efficiency, both in time and energy use. During the initial development of high-speed trains, much of the focus was improvements of electric motors and the reduction of frame weight, rather than improved train aerodynamics. Indeed, progress in these two areas has resulted in a remarkable speed increase over the past decades. The aerodynamic performance of a HST, which was of less importance when travelling at lower speeds, now becomes a limiting factor as speed is further increased. Specifically, for a train travelling in the open-air without cross-winds, good aerodynamic performance means both the minimisation of aerodynamic drag and the induced disturbance to the surrounding air. This flow disturbance induced by the passing of a HST is known as slipstream, which is a combined effect of multiple flow features: the head pressure pulse, boundary-layer development along the train body, flow under the bogies and the wake behind the train.

* Corresponding author.
E-mail address: shibo.wang@monash.edu (S. Wang).

https://doi.org/10.1016/j.jfluidstructs.2018.03.013
0889-9746/

Research into investigating the aerodynamic characteristics of bogies has mainly been initiated for the following two reasons. Firstly, the bogies are a significant source of aerodynamic drag; thus, improving their aerodynamic performance is beneficial to energy efficiency. For example, for a streamlined HST travelling at cruising speed, aerodynamic resistance contributes to 75%∼80% of the total resistance, and 38%∼47% of that is caused by the bogies and associated interference drag (Raghunathan et al., 2002). Therefore, measures have been applied to optimise bogies for drag reduction. Mancini et al. (2001) showed that installing fairings on the existing bogies of an ETR 500 HST could reduce the drag by approximately 10%, and further reduction was expected by retrofitting the bogies. Secondly, the bogies can significantly alter the underbody flow, which is strongly correlated with the *ballast flight* phenomenon. The underbody flow can be characterised as a turbulent Couette flow, and García et al. (2011) have proposed an analytical solution for a simplified case. By studying a more realistic train model, Kaltenbach et al. (2008) reported that the ideal Couette flow could be regularly interrupted by the passing bogies and inter-carriage gaps. For example, the "funneling" of the flow into the rear of the first bogie cavity can introduce a strong secondary flow structure and further affect the downstream flow. As shown in Kaltenbach et al. (2008), the underbody flow is strongly dependent on the geometry of the bogies; Jönsson et al. (2014) explicitly studied the bogie effect by comparing the underbody flow with and without bogies. The comparison concluded that the bogies significantly increased the velocity, velocity gradient and turbulence intensity of the underbody flow (Jönsson et al., 2014). Ballast flight, where ballast particles become airborne during the passage of a train, is due to the combined effect of mechanical and aerodynamic loadings (Quinn et al., 2010). Therefore, fluid acceleration caused by the bogies could worsen the ballast flight phenomenon (Quinn et al., 2010). Specifically, Soper et al. (2017) determined that bogies significantly alter the horizontal instead of vertical velocities, and concluded that any effects on ballast flight are likely to occur from a shear-type flow. Additionally, the alteration to the underbody flow is also profound under crosswind conditions. Cooper (1981) determined that under cross-wind conditions, the bogies partially blocked the underbody flow and introduced a strong local pressure field, which resulted in a significant increase in the forces and moments. Copley (1987) further investigated the mechanisms affecting the aerodynamic loading, and discovered that without the bogies, the vortical wake was like a three-dimensional *Karman Vortex Street*, with vortices being shed from successive points on both the roof and the under side of the train. However, when wheels were simulated, the vortices shed from the underside of the train were disrupted and reduced in strength, which increased the overall force components on the train (Copley, 1987).

As can be seen from these investigations, the bogie effect has been investigated mainly either to determine the aerodynamic loading exerted on the train surface for the purpose of drag reduction, or to determine the alteration to the local underbody flow for the purpose of ballast flight analysis. In comparison, less research has been undertaken on bogie effects on HST slipstream, and especially on the wake structures. By studying the slipstream of a full-scale HST, Pii et al. (2014) identified the development of left-to-right pressure fluctuations along the train, which were caused by the presence of the bogies, and further inferred that the bogie-induced fluctuations actually trigger the wake's spanwise motion. Alternatively, from the correlation between the pressure fluctuation at the side surface of the tail and the wake's spanwise motion, Bell et al. (2016a) proposed that the origin of the spanwise motion could also be vortex shedding from the tail, although this does not necessarily rule out the bogie generation hypothesis.

The spanwise oscillation of a HST wake has been identified as a typical HST slipstream characteristic, but its initiation is still not fully understood. Reviewing the methodologies used to study HST slipstream through computational analysis indicates that numerical set-ups, both with bogies (Muld et al., 2012a; Yao et al., 2013) and without bogies (Östh et al., 2015; Pereira and André, 2013), have been adopted. However, since the effects of bogies on HST slipstream characteristics are not yet fully understood, this makes to it unclear what the effect on predictions will be if bogies are ignored. Specifically, the impact on the wake caused by the presence of the bogies have not been fully documented and characterised, and this is the rationale for undertaking the current study.

Therefore, effort is needed to understand and quantify the effects of bogies on HST slipstream characteristics, for example, the causes of spanwise oscillation of the wake. To isolate the bogie effects, this study systematically studies and compares the slipstream characteristics of two otherwise identical generic train models, with the only difference being whether the bogies are fully featured. Unlike previous studies, which mainly focused on ballast flight or drag reduction, the current study investigates bogie effects from a slipstream perspective. For this reason, the flow field is naturally divided into two regions: the flow development region (covering the length of the train) and the wake region, and the effects of bogies on each region are studied and discussed separately. Beyond this, the influences on slipstream velocity assessment and aerodynamic loading are also investigated.

2. Methodology

2.1. Geometry

The numerical train model used in this study is based on the 1/10th *Deutsche Bahn Inter-City-Express 3* (ICE3) high-speed train model, which is a widely operated train model in European and Asian countries. ICE3 has a representative HST external shape, and its Computer-Aided Design (CAD) model is freely available from the DIN Standards Railway Committee (DIN Standards Committee Railway, 2018). This makes ICE3 an ideal HST model for train slipstream investigation.

To achieve the primary aim of explicitly studying the effects of bogies on HST slipstream characteristics, two numerical models are constructed: a *Simplified Train Model* (denoted as Model 1, or M1) and a *Full-featured Train Model* (denoted as

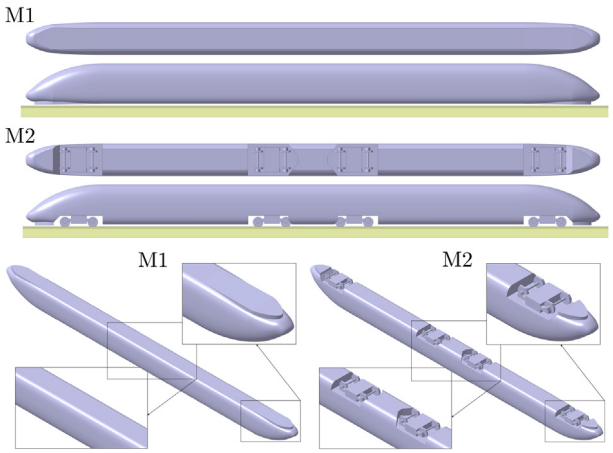

Fig. 1. The comparison between the underbody structure between the flat-underbody model and the full-featured model.

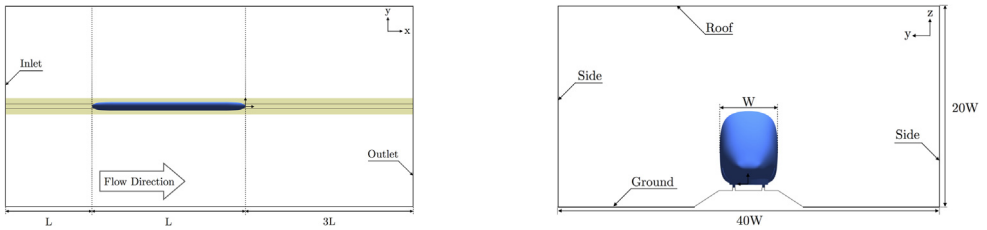

(a) Top view. (b) Front view.

Fig. 2. Schematics of the computational domain: (a): top-view; (b): front-view (Not to scale).

Model 2, or M2), as illustrated in Fig. 1. The overall geometrical features of the two models are identical; for example, the length-width-height ratio of approximately 50:3:4, the ground clearance of 381 mm (in full-scale), and the inclusion of a snowplough. The only difference between M1 and M2 geometries is that the former covers the bogie-sets with a flat surface, while the latter includes four bogie-sets. For implementing this fundamental investigation, the bogie-sets have been simplified by only retaining the generic large-scale geometric features including the axles and wheels, but omitting fine-scale geometry details; there are studies in the literature that have considered more realistic bogie-sets, e.g., Kaltenbach et al. (2008) and Sima et al. (2008). The comparison of the underbody structures between M1 and M2 is highlighted in Fig. 1. The numerical train model is positioned on a single-track ballast configuration. The dimensions of the ground configuration are specified according to CEN guidelines (European Committee for Standardization (CEN), 2009). Compared with the dimensions specified by CEN (European Committee for Standardization (CEN), 2009), the thickness of the rails is extended from 50 mm to the wheel width of 135 mm (in full-scale) in order to represent a realistic contact between the rails and wheels.

2.2. Computational domain and boundary conditions

The layout of the computational domain is identical for both cases, for which the train model is positioned on a single ballast track in a computational domain consisting of hexahedral elements, and the ballast is extended through the entire domain, i.e., from the inlet to outlet. Therefore, a cross-section through the computational domain for M2 is used as an example here to illustrate the numerical set-up, with its schematic presented in Fig. 2. For the discussion, spatial dimensions are generally normalised by the train width (W) in the spanwise direction (y-direction), or by the length (L) of the train in the streamwise direction (x-direction). The origin of the coordinate system is positioned in the spanwise mid-plane, at the height of the top surface of the rails, with $x = 0$ corresponding to the tail tip.

The boundary conditions are tabulated in Table 1. A uniform velocity boundary condition with a turbulence intensity of 1% is applied at the inlet. The Reynolds number (based on W) is 7.2×10^5. These values are chosen for consistency for a comparison with wind-tunnel experiments, but noting that they are not representative of a full-scale train operation. A zero static pressure condition is applied at the outlet boundary. A no-slip wall boundary condition is applied to all train surfaces, except for the wheels, which is not applicable for M1. Symmetry boundary conditions are applied at the top and

Table 1
The list of boundary conditions.

Boundary conditions	Simplified train model (M1)	Full-featured train model (M2)
Train surfaces	No-slip stationary wall	No-slip stationary wall
Wheels (include axles)	N/A	No-slip rotational wall
Ground	No-slip moving wall	No-slip moving wall
Inlet	Uniform velocity	Uniform velocity
Outlet	Zero static pressure	Zero static pressure
Sides and roof	Symmetry	Symmetry

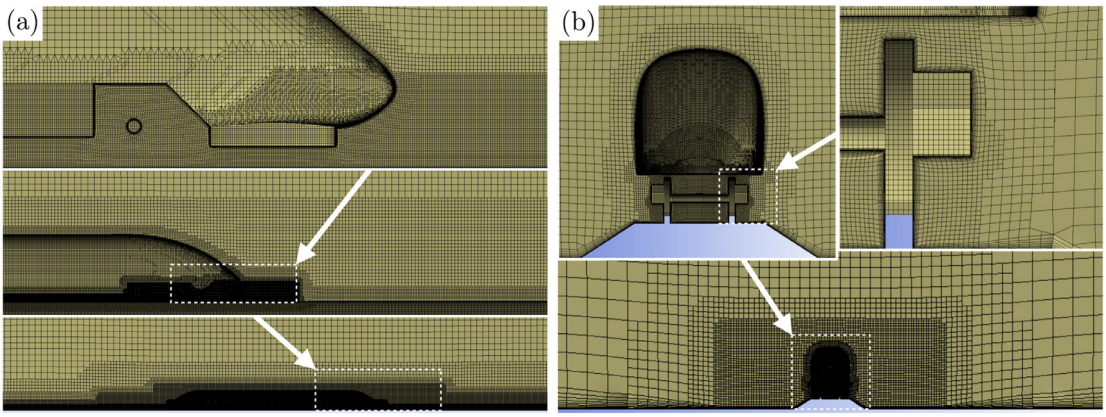

Fig. 3. The visualisation of grid refinement around the train based on M2: (a): centre-plane; (b): cross-section.

sides of the computational domain. Note that for a clearer visualisation of the computational setup and domain dimensions, Fig. 2 is not drawn to scale. To simulate the realistic condition of a moving train travelling through still air, where no relative motion exists between the air and the ground, a no-slip moving-wall condition at the freestream velocity (U_∞) is applied to the ground, including the ballast and rails. The axes of the rotating wheel-sets are along the centrelines of the axles, and the wheels rotate at a constant angular velocity, with the speed at the rim equal to the speed of the moving ground. All no-slip wall boundaries, including the train and ground, adopt default roughness parameters (i.e. the Roughness Height and Roughness Constant of 0 and 0.5 respectively), which represent a smooth wall condition (Fluent, 2006). Obviously in the full-scale scenario, the roughness of the train surface and ground is different and may alter the local flow field near the wall, especially when we take the sleepers into consideration. However, as a preliminary study focusing on the effects of bogies on slipstream and wake, the potential influences due to wall roughness are isolated by applying an identical value for M1 and M2.

2.3. Meshing strategy

The two models use an identical meshing strategy, which is based on the predominately-Cartesian *cut-cell* approach, allowing substantially increased mesh concentration around the train and in the wake, together with a relatively smooth transition to lower resolution away from the train. This mesh concentration is accomplished by applying virtual refinement zones at target regions. For example, in this study, multiple levels of refinement zones are utilised to achieve higher accuracy around the train and within the wake, as illustrated in Fig. 3. To ensure all important flow features are captured, the dimensions of the refinement regions were determined based on preliminary simulations. This method achieves a high uniform resolution in the slipstream measurement regions, and aids in accurately capturing the boundary layers and induced-flow separation generated by smaller-scale geometrical features. *Inflation layers* are applied to all wall boundaries to capture the boundary layer development. A smooth transition is established between adjacent cells, including between the outer inflation layer and the hexahedral grid, and at the interface of two refinement zones, as illustrated in Fig. 3.

A mesh independence study was undertaken in a previous related study (Wang et al., 2017) examining the effect of different turbulence models on slipstream prediction. In that study, the performance of three sequentially refined grids (coarse, medium and fine) for predicting HST slipstream were evaluated, showing that drag and slipstream predictions varied by less than 1% and 2% between the fine and medium grids. This study adopts the equivalent mesh settings of the fine grid, for which the key meshing parameters are listed in Table 2. Based on these settings, the number of cells for M1 and M2 is 25.1 and 27 million, respectively.

Table 2
Key meshing parameters.

Cell size	Train surface mesh	$0.00625H$∼$0.025H$
	Under-body refinements	$0.00625H$∼$0.0125H$
	Wake refinements	$0.0125H$∼$0.05H$
	Far-field refinements	$0.1H$∼$0.4H$
No. of inflation layers		10
Train surface wall y^+		1∼20

2.4. Solver description

The numerical solver utilised in this research is the commercial CFD code *FLUENT*, which is part of the ANSYS 16.2 software suite. A pressure-based transient solver is utilised for predicting the highly turbulent flow. *Detached Eddy Simulation* (DES) is used to capture the large-scale turbulent flow structures, and specifically, a variant know as *Improved-Delayed DES* (IDDES) is utilised in this study. DES is a hybrid turbulence model that blends Reynolds-Averaged Navier–Stokes (RANS) modelling near boundaries with Large Eddy Simulation (LES) for the outer flow. IDDES is a type of DES model that applies an *improved delayed shielding function* to achieve a higher accuracy within the RANS-LES blending region. This also improves the wall-modelling capability. Similar to the classic DES blending technique, IDDES also utilises RANS to approximate the boundary layer and applies LES to capture the time-dependent turbulent flow away from boundaries. *Shear-Stress Transport* (SST) $k-\omega$ model is used for the RANS part within the IDDES model, due to its superior performance on modelling the near-wall boundary-layer regions with undefined separation points. IDDES has been extensively adopted to study the train aerodynamics, for example, the study of the slipstream assessment (Huang et al., 2016) and underbody flows (Zhang et al., 2016). A fuller description of the IDDES model is given in Spalart (2009). To start the time-dependent simulation, the flow field is initialised with a second-order accurate steady-state RANS simulation based on the SST-RANS model. The flow is then solved with the IDDES turbulence model.

The solver timestep was chosen as $0.0025T_{ref}$ to maintain the Courant number of typical smallest cells less than unity, which is suggested for DES-type simulations. Because of this, the *Fractional-Step Scheme* with *Non-Iterative Time Advancement* can be used to integrate forward in time. The *bounded second-order implicit* formulation is applied for transient simulations. For the spatial discretisation, except for the momentum equation for which *bounded central differencing* is utilised, all other flow equations are discretised with the *second-order upwind scheme*. Unsteady statistics results are collected after the flow field has reached an asymptotic statistical state, which is checked through comparisons with predictions from shorter averaging periods. It is useful to define a reference time scale based on the train height and freestream velocity given by $T_{ref} = H/U_\infty$. Unsteady statistics are sampled over 195 T_{ref}. This is equivalent to the time taken for the fluid to advect through the entire domain 3 times, or to pass the length of the train approximately 15 times.

2.5. Validation

Validation of the numerical model was presented in a previous study (Wang et al., 2017), which systematically evaluated the effects of the key numerical settings for predicting the slipstream, including the selected turbulence model, the grid resolution and the time-step, and provided guidelines for selection of those settings. The current research utilises the best choice numerical setting derived from that study (Wang et al., 2017). The validation was carried out by comparing the results of time-averaged and dynamic flow features between numerical simulation and wind-tunnel experiments (Bell et al., 2016a, b). As an example, the slipstream profiles obtained from the experimental measurements and numerical simulations are plotted in Fig. 14. The wind-tunnel experiment was conducted in the Monash University 1.4 MW closed-circuit wind tunnel, and a full description regarding the experimental set-up and results can be found in Bell et al. (2017). The geometry in this current study is identical (M2) or even simpler (M1) than that used for the validation study, and the flow conditions are very similar. However, the ground boundary condition varies: the previous study utilised a stationary ground configuration to replicate the wind-tunnel experimental environment, while this study adopts a moving ground configuration to match the actual relative velocity between the ground and the train. The feasibility of applying the present numerical method on resolving the slipstream with different ground conditions has been verified by the authors in another study (Wang et al., 2018), and the flow changes that are introduced by the stationary ground boundary layer were investigated and documented as well. According to that study (Wang et al., 2018), the moving-ground condition of this study eliminates the ground boundary layer development and growth. The underlying assumption is that numerical settings that are capable of capturing the growth of the ground boundary layer and its interaction with the train-induced wake structures, are also appropriate for the simpler case in which the stationary ground boundary layer is not present.

3. Results and analysis

This study investigates the effects of bogies from three perspectives: *wake flow structure* (Section 3.1), *slipstream assessment* (Section 3.2) and *aerodynamic loading* (Section 3.3). To begin with, the influence of the bogies on slipstream

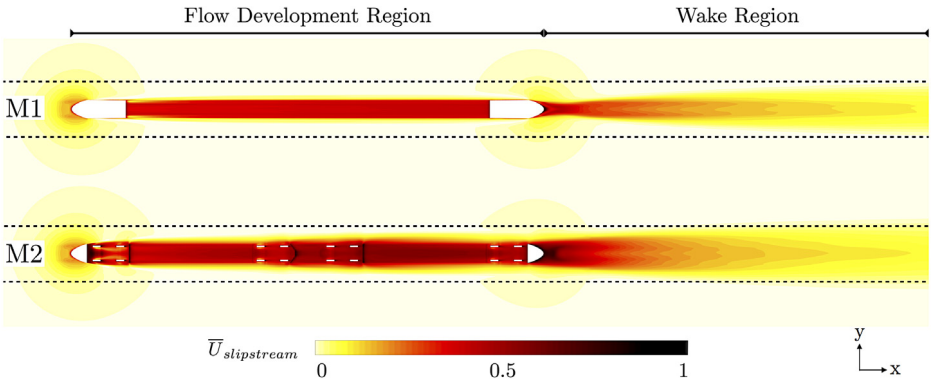

Fig. 4. Classification of the two flow regions visualised by $\overline{U}_{slipstream}$ at $z = 0.05H$, and the slipstream assessment location is represented by the dotted lines.

development is investigated, in terms of statistical wake-flow features and wake dynamics. Following that, how the altered wake flow further alters slipstream measurements is studied in accordance with Technical Specifications of Interoperability (TSI) specification. The TSI specification is issued by the European Railway Agency, which provides guidelines for the trains operating across European countries. Lastly, the impact of the bogies on the overall aerodynamic force components is presented by comparing the train surface pressure between two models.

3.1. Flow structures

The strength of slipstream is quantified by the slipstream velocity ($U_{slipstream}$), which is defined through the *horizontal* components of train-induced air movement. As slipstream velocity is defined in a ground-fixed (GF) stationary reference frame, while CFD simulations are based in the train-fixed (TF) reference frame; thus a change of frame is required. Therefore, $U_{slipstream}$ is defined by

$$U_{slipstream} = \sqrt{\left(U_{GF}^2 + V_{GF}^2\right)}, \tag{1}$$

where

$$U_{GF} = U_\infty - U_{TF}, V_{GF} = V_{TF}. \tag{2}$$

In Eqs. (1) and (2), the subscripts *GF* and *TF* indicate *ground-fixed* and *train-fixed* reference frames, respectively. Velocities, including slipstream velocities, quoted in this study are typically normalised by the freestream velocity (U_∞). Again, note that slipstream is only based on the downstream (U) and transverse (V) components of the velocity, while the vertical velocity component is ignored. According to the TSI specifications (European Union Agency for Railways, 2014), the slipstream velocity measurement should be undertaken 3 m (in full-scale) away from the centreline of the train and at two different heights, i.e. trackside height ($z = 0.05H$) and platform height ($z = 0.35H$).

To explicitly study the effects of bogies as the slipstream develops, the flow field is divided into two regions: the flow development region (covering the train) and the wake region. A schematic of the two regions is illustrated in Fig. 4, based on the time-averaged slipstream velocity ($\overline{U}_{slipstream}$) at the trackside height, and the black dotted-lines represent the slipstream assessment location under TSI specifications.

The *flow development region* extends from the train head to the tail, and the wake region starts from where the wake structures separate from the tail to the downstream location where slipstream becomes negligible. The flow development region covers where there is direct local disturbance caused by the presence of bogies, and the wake region focuses on how the altered upstream flow influences the formation and propagation of the wake structures. However, note that as the slipstream development along the train is a continuous process, there is no definite boundary between the two regions. This is especially true around the tail, where the wake structures are formed and separate from the train surface. Fig. 4 shows that the bogies increase the underbody slipstream velocity, and widen the wake behind the train. A detailed analysis of the bogie effect in each region is presented in Sections 3.1.1 and 3.1.2.

3.1.1. Flow development region

Unsurprisingly, the flow development region is identified as the region where the flow develops as it passes over the HST, arbitrarily taken from the nose to the tail. The bogie influence within this region is visualised in Fig. 5 by the turbulent kinetic energy (TKE), and the time-averaged y-vorticity ($\overline{\omega}_y$), in the vertical spanwise centre-plane.

As can be seen in Fig. 5, the bogies within this region only locally alter the underbody flow, while the flow over the upper train surface remains almost unaffected. The mechanism of the bogies interfering with slipstream development is to alter

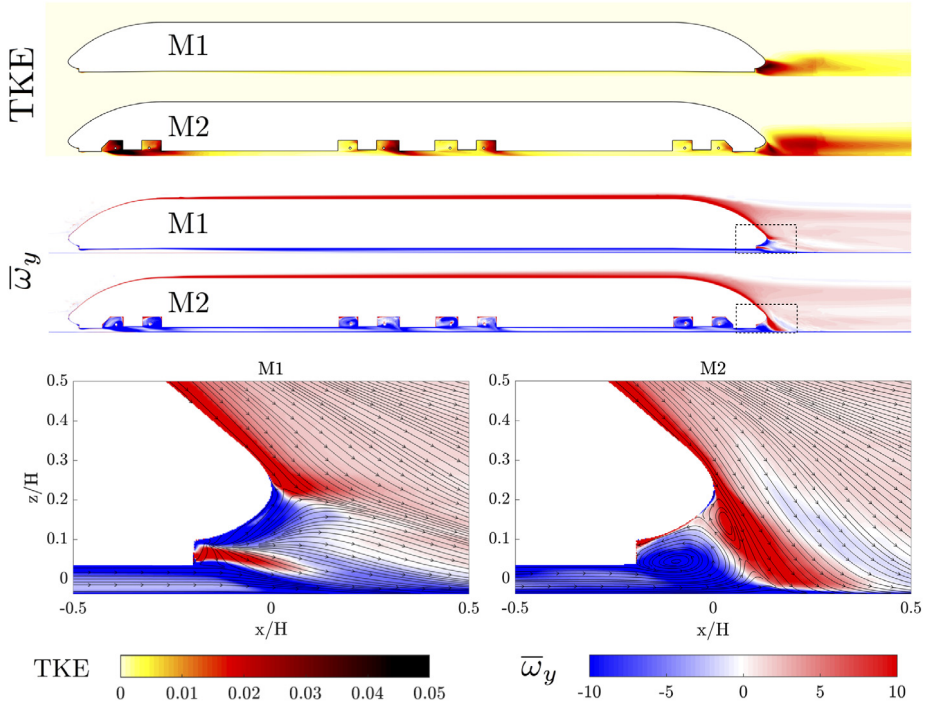

Fig. 5. The bogies effects within the flow development region illustrated by TKE and $\overline{\omega}_y$ with in-surface projected velocity streamlines at $y = 0W$.

the underbody flow by restricting it through blockage, and to increase the TKE level through flow separation from the bogies. According to the TKE contours in Fig. 5, the bogies not only locally increase the turbulence level around the bogies, but also the effect advects into the wake.

For the time-averaged flow features, an identical boundary layer growth is seen by the positive $\overline{\omega}_y$ layer over the train top surface. In contrast, a significantly altered underbody flow is apparent. A thin boundary layer develops on the flat bottom surface in M1, while the bogies introduce high local $\overline{\omega}_y$ magnitude regions in M2. The main downstream alteration to the flow caused by the bogies is identified between the train tail tip and ballast, which is highlighted by $\overline{\omega}_y$ and time-averaged in-surface projected velocity streamlines in the lower images of Fig. 5. This figure illustrates that a pair of coherent time-averaged recirculation regions are formed in M2, while these do not occur in the M1 near wake. A possible explanation for this is that the twin vortices are formed due to the significant kinetic energy difference between the strong downwash from the train top surface and low-speed underbody flow. Specifically, the lower energy fluid passing under the train is not sufficient to prevent the high-energy fluid passing over the train separating at the trailing nose. Combined with separation of the underbody flow at the snowplough, this leads to the two local counter-rotating recirculation regions. In comparison, the high momentum underbody stream in M1 is sufficient to cause the flow to remain attached to the point of the trailing nose.

3.1.2. Wake region

The *wake region* is defined as the region downstream of the tail, where the vortical flow structures that separate from the train surface propagate downstream. Consistent with wind-tunnel experimental results (Bell et al., 2016a, b), the dominant time-mean wake structure is a pair of longitudinal counter-rotating vortices.

In this study, it makes sense to further divide the development and evolution of the wake into two sub-regimes: the *wake-formation regime* and the *wake-propagation regime*, in accordance with the formation and evolution of the time-mean coherent longitudinal vortical structures as illustrated in Fig. 6.

The development of the time-mean and instantaneous wake structure behind the tail is depicted through an iso-surface of the *Q-Criterion* ($Q = 2$) in Fig. 6, where positive Q highlights rotation-dominated flow structures. Additionally, to indicate the origin of the longitudinal vorticity in the trailing vortices, the Q-criterion iso-surface is coloured by x-vorticity (ω_x). The streamwise vorticity is calculated based on the normalised spanwise and transverse velocities. The instantaneous flow structures in the right-hand column of Fig. 6 illustrate that the turbulent wake structures are more concentrated towards the centreplane when they are separated from the tail of M1, while the bogies introduce multi-scale flow structures at a higher turbulence level. According to the comparison between the time-averaged flow structures in Fig. 6, the alteration to the underbody flow significantly affects the near-wake formation of the time-mean wake vortices. In M2, the downwash

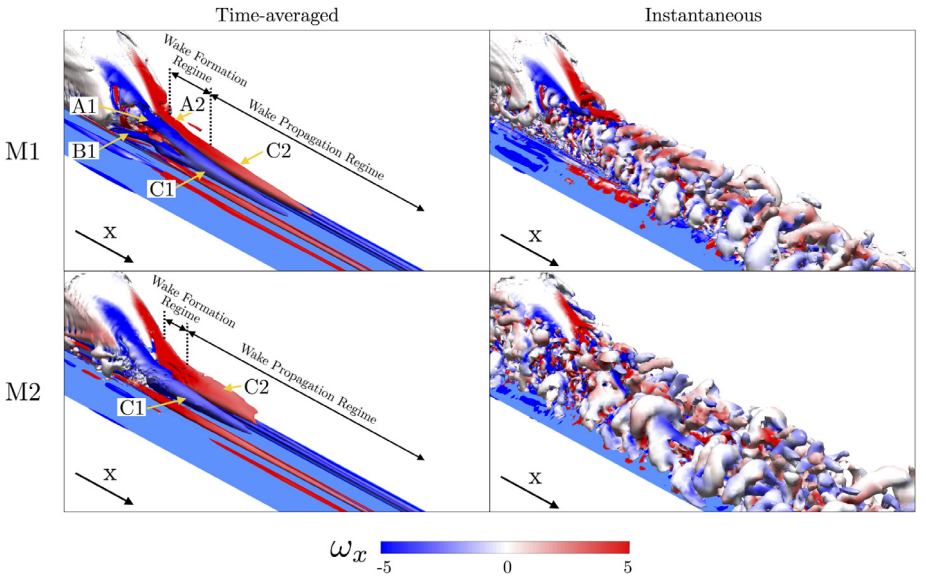

Fig. 6. The comparison of the bogie effects on the development of the wake structure at the tail, visualised by an iso-surface of Q-criterion coloured by ω_x.

from the tail dominates the underbody stream, and generates a pair of longitudinal trailing vortices (denoted as vortex pair C) behind the tail. This pair is a coherent, persistent wake structure, and initiates from the curved edge between the top and side surfaces of the tail, in a similar way to the (C-)pillar vortices identified in vehicle aerodynamics. Additionally, from the $\overline{\omega}_x$ contours, it can be seen that the longitudinal vorticity of the trailing vortices originates from the twisting effect at the C-pillar, which is caused by the pressure difference between the tail side and top surface. This is further illustrated in Section 3.3. In comparison, with the flat underbody configuration (M1), apart from the primary pillar vortices (denoted as vortex pair A), a pair of secondary vortices (denoted as vortex pair B) is formed at the snow-plough due to the higher momentum streamlined underbody flow. Note that vortex B2 is not visible in Fig. 6 as it is behind vortex A2. As the wake propagates downstream, the two vortex pairs, A and B, meet at approximately $x = 1H$, and then merge into one vortical structure (denoted as vortex pair C), which is analogous to the coherent trailing vortices in M2. Beyond this point, the wake structures of M1 and M2 are qualitatively identical.

The formation and propagation of the time-averaged wake structures are quantitatively depicted by $\overline{\omega}_x$, in-surface projected velocity vectors and the vortex boundaries, on six consecutive vertical planes between $x = 0.5H$ and $5H$, as presented in Fig. 7. As the time-averaged flow structure is symmetric about the mid-plane, only the left half of the flow field is presented. The boundary of the trailing-vortex structure is depicted through an iso-line of $\Gamma_2 = 2/\pi$, which is a method often chosen by experimentalists to mark the extent of a vortex-dominated region (Graftieaux et al., 2001). In addition, the core of a vortex is indicated by a green asterisk, which is determined by the maximum local value of Γ_1 (again see Graftieaux et al., 2001). The crosses ("+") and circles ("o") in Fig. 7 represent the trackside ($z = 0.05H$) and platform ($z = 0.35H$) slipstream measurement location respectively, based on the TSI specifications (European Union Agency for Railways, 2014).

According to Fig. 7, when the bogies are included, a pair of trailing vortices (C) is formed immediately behind the tail ($x = 0.5H$), and as it propagates downstream, it rolls over the rails and moves away from the spanwise centre-plane. In comparison, two discrete pairs of vortices (A and B) are identified at $x = 0.5H$ in M1, and they start to merge to form a single vortical structure (C) at $x = 1H$. This description is consistent with the wake-structure evolution illustrated in Fig. 6. In comparison with M2, M1 shows that vortex pair C stays closer at the centre-plane. Additionally, as the underbody stream pushes against the downwash vortex A, and the cores of C in M1 are slightly shifted upwards.

In this study, the strengths of vortices are quantified through the circulation, which is calculated by the surface integral of $\overline{\omega}_x$ within the vortex boundaries using *Stokes' Theorem*. The strengths of vortex A and B in M1 are $1.41 \times 10^{-3} U_\infty/H$ and $1.02 \times 10^{-3} U_\infty/H$, respectively. This indicates that the downwash vortices formed from the top surface are approximately 32.1% stronger than the vortices generated from underneath. For completeness, the strength of coherent counter-rotating vortex pair C is described by the mean vortex circulation at $x = 2H$, which is $2.24 \times 10^{-3} U_\infty/H$ for M1 and $3.41 \times 10^{-3} U_\infty/H$ for M2. This shows that the bogies can alter the strength of trailing vortices by about 30%.

The decay of the wake structure is quantified by the change of $\overline{\omega}_x$ at the vortex core, and the results are plotted in Fig. 8. Fig. 8 shows that M2 has a significantly higher decay rate within the near-wake compared to that further downstream. This is expected due to the higher turbulence level caused by the perturbations from the bogies. Note that the core vorticity $\overline{\omega}_x$ for M1 model between $x = 1$ and $3H$ cannot well represent the vortex strength as the coherent single vortex pair C is not yet fully formed.

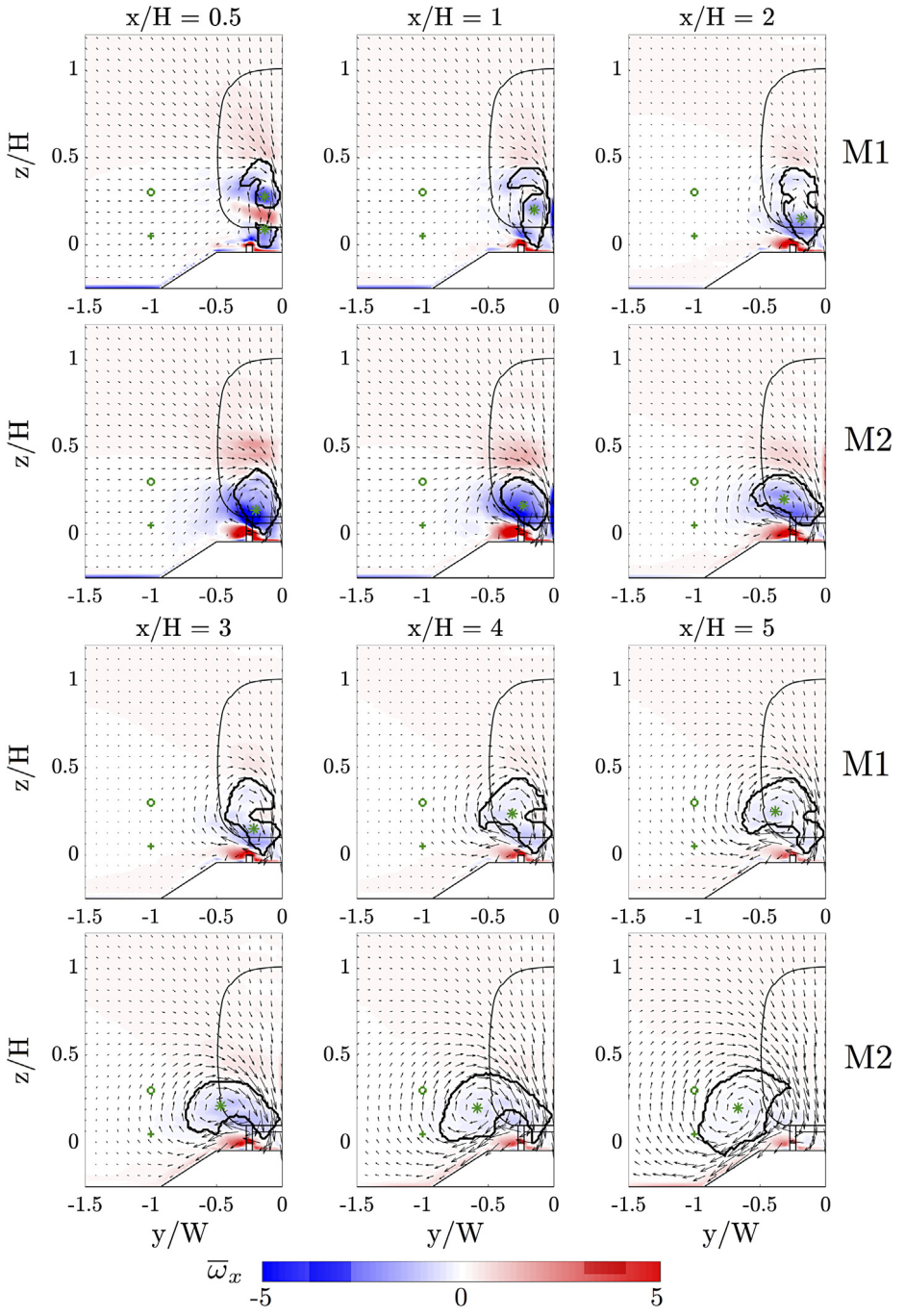

Fig. 7. The comparison of the wake development downstream based on six consecutive vertical planes between $x = 0.5$ and $5H$. Here, "∘": platform slipstream assessment location; "+": trackside slipstream assessment location. The vortex boundaries, shown by the black lines, are identified by the Γ_2 criterion. The vortex centres ("∗") are identified using local maximum values of Γ_1 (see Graftieaux et al., 2001).

In the following, the dynamics of the near-wake flow structures, i.e. vortex pairs A, B in M1, and the vortex pair C in M2, are investigated based on the static pressure in the vortex cores at $x/H = 0.5$. The core coordinates ([y-coordinate, z-coordinate]) for vortex A, B and C at $x/H = 0.5$ are ($[\pm 0.133W, 0.275H]$), ($[\pm 0.133W, 0.0875H]$) and ($[\pm 0.2W, 0.1375H]$), respectively. The frequency spectra and cross-correlation coefficients between adjacent structures are illustrated in Fig. 9, where the frequency is quantified by the non-dimensional Strouhal number (St_W) based on the train width (W).

According to the power spectral density (PSD) profiles in Fig. 9(a), the pillar vortices, i.e. vortex pair A in M1 and vortex pair C in M2, demonstrate identifiable dominant frequencies of 0.75 and 0.58, respectively. In comparison, the lower vortex

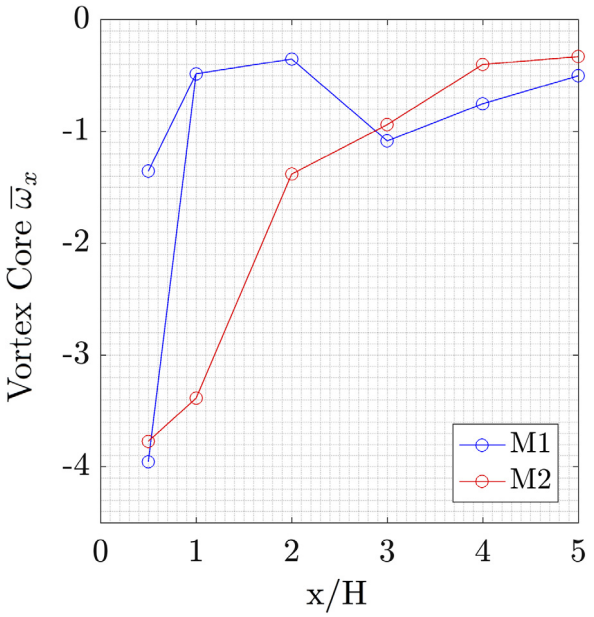

Fig. 8. The comparison of the wake decay rate based on the change of vortex core $\overline{\omega}_x$.

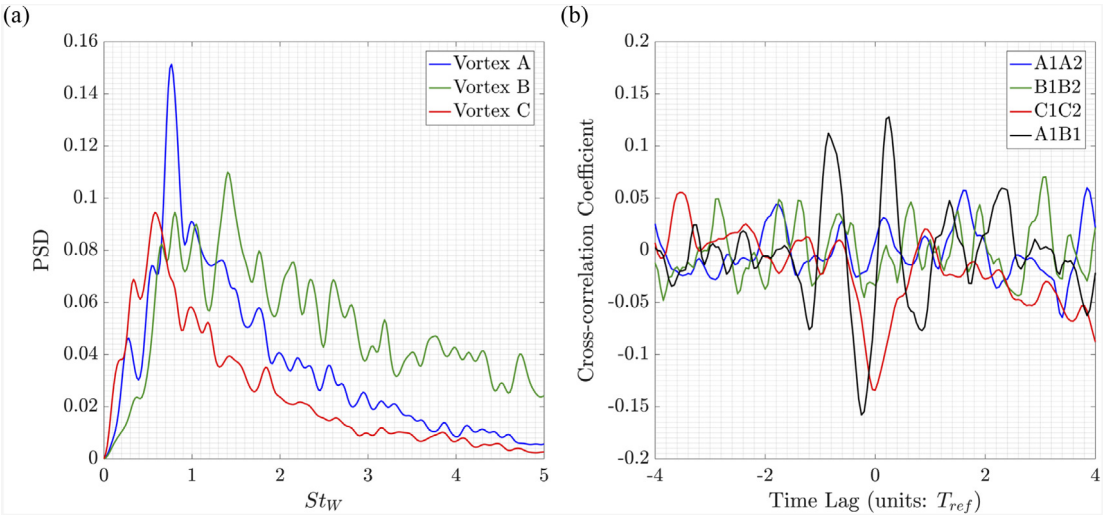

Fig. 9. The comparison of dynamic response of the near-wake structures: (a): the frequency content within the vortex cores; (b): the correlation between the vortex structures. Note here the vortex pairs A, B are in M1, and the vortex pair C is in M2.

pair B in M1 shows a broad frequency response without a clear peak frequency. In addition to the frequency responses of individual structures, the interactions between two adjacent structures are studied by the cross-correlation between the core pressure, and the results are presented in Fig. 9(b). The cross-correlation coefficient of 1 represents an in-phase motion, while -1 indicates an out-of-phase motion. The time-lag is normalised by T_{ref}. This figure indicates that for each vortex pair, no significant correlation exists for vortex pairs A and B of M1; however, the trailing vortex pair C of M2 shows a strong out-of-phase correlation. This implies that the spanwise wake oscillation is initiated immediately behind the tail in M2, while it is not established in either vortex pairs in M1, even for the equivalent-origin downwash pillar vortex A. On the other hand, a strong correlation with a $\pi/2$ phase difference is identified between the legs of the pillar vortex pair A and secondary vortex B beneath. This implies that the higher and lower vortices of M1 on the same side demonstrate a stronger vertical dependency, even though there is no spanwise dependency.

Additionally, the dynamic wake features can be understood through Proper Orthogonal Decomposition (POD), especially the detailed makeup of transient wake structures. This study utilises the Snapshot POD method, initially proposed by Sirovich

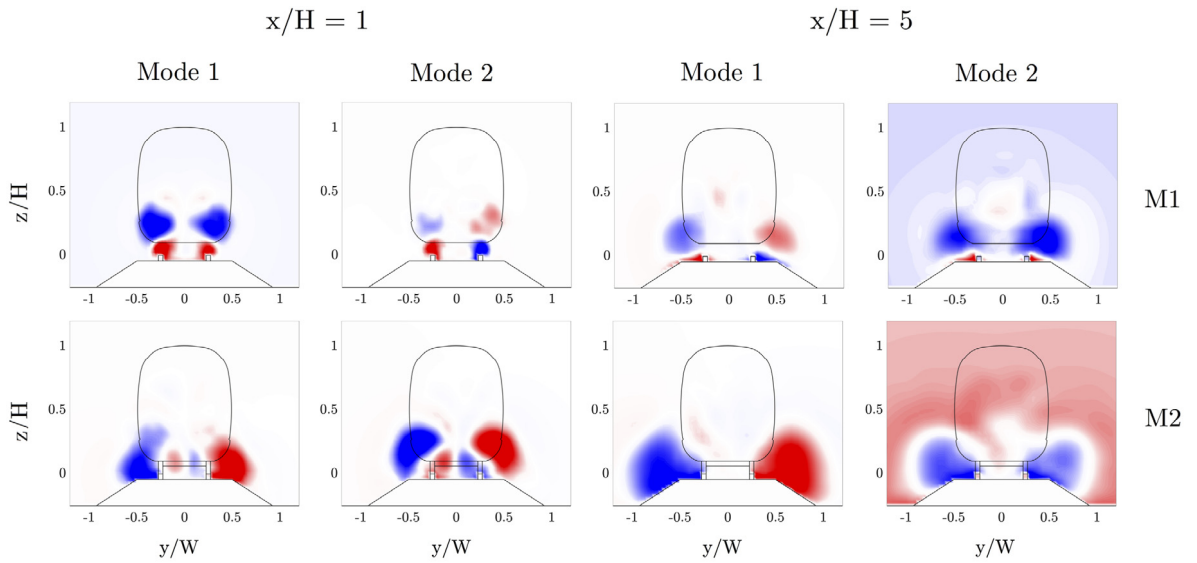

Fig. 10. The comparison of dominant transient wake features resolved by POD for the near- and intermediate-wake region.

(1987), due to its strength in extracting coherent flow features (denoted as modes), from a turbulent flow field, and ranking them according to their energy proportion. In this study, the components of the dominant transient flow features at the near- and intermediate-wake region are illustrated by the two most energetic POD modes resolved at $x/H = 1$ and 5. The POD analysis in the current study is based on the total pressure.

Fig. 10 shows that the dominant transient feature within the M1 wake formation region is a simultaneous energy increase/decrease centred on the vortices, corresponding to a longitudinal pulsing of the vortices. Additionally, the impulses of the vortex A and B are out-of-phase, which represents a vertical energy fluctuation. The second energetic mode depicts an out-of-phase oscillation within each vortex pair, which associates with the left-to-right oscillation. In comparison, both modes in M2 within the near-wake region are associated with the spanwise energy fluctuation. In the intermediate-wake region ($x = 5H$), the first two most energetic modes between M1 and M2 become qualitatively identical, which are an out-of-phase spanwise oscillation and an in-phase wake pulsing. Quantitatively, M2 shows a larger energy fluctuation region due to the wider unsteady wake.

Additionally, the effect of the bogies on the downstream wake development, especially on the spanwise wake oscillation, is studied based on a horizontal plane at a height at $z = 0.15H$, as shown in Fig. 11. The instantaneous flow structures are visualised by contours of $U_{slipstream}$ at an arbitrary time instant.

Firstly, the coherence of the spanwise oscillation is quantitatively described by the cross-correlation of the lateral velocity component (V_{GF}) based on an array of points from $x = 0 \sim 10H$ that are plotted as white circles in Fig. 11. The cross-correlation is calculated between each pair of points that are symmetric across the centreplane at $0.33W$ apart, and the downstream distance between two adjacent pairs is $0.25H$. Hence, a total of 50 pairs between $x = 0$ and $10H$ are utilised to capture the development of the wake's spanwise motion with downstream distance, and the cross-correlation profiles for each pair along the longitudinal direction are illustrated in Fig. 12(a).

As the profiles of cross-correlation coefficient against time lag are symmetric at zero time lag, only the positive time lag portion is presented. According to Fig. 12(a), a peak cross-correlation coefficient is determined at zero time lag (except for the pairs within the wake formation region of M1), and its positive value implies the spanwise oscillation. Therefore, the cross-correlation coefficients at zero time-lag for the pairs ranging from $x = 0$ to $10H$ are plotted in Fig. 12(b) for a quantitative description of the coherence of spanwise motion for the wake. Fig. 12(b) shows that without the bogies, the spanwise oscillation cannot be identified until approximately $x = 4H$. This is consistent with the wake dynamics, as illustrated in Figs. 9 and 10, in which the dominant transient feature within the M1 wake formation regime is the vertical interaction between primary pillar vortices (vortex pair A) and secondary vortices (vortex pair B) beneath, instead of a spanwise oscillation. As the wake propagates downstream after the formation of vortex pair C, the spanwise correlation between the trailing legs then gradually develops. In comparison, the spanwise wake oscillation is immediately established behind the tail for M2, which is coincident with the formation of twin vortices immediately in the near wake. This indicates that spanwise motion can be identified in both cases once the vortex pair C is properly formed, regardless the presence of the bogies. Together with the similar spanwise oscillation frequency in both cases, this suggests that the bogies are not the ultimate cause of the spanwise oscillation, instead, the wake oscillation is an intrinsic convective instability of the trailing vortices.

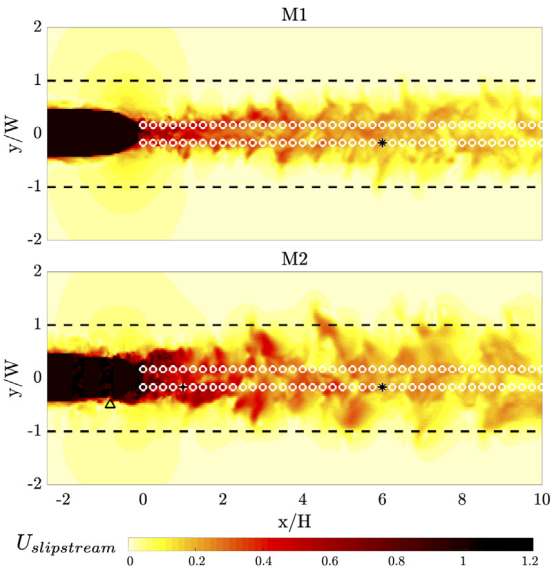

Fig. 11. The wake propagation visualised by the instantaneous $U_{slipstream}$ ("∘": an array of point pairs for spanwise motion identification; "△": the probe for measuring the shedding from the bogie; "+": the probe for measuring near-wake dynamics; "∗": the probe for measuring intermediate-wake dynamics).

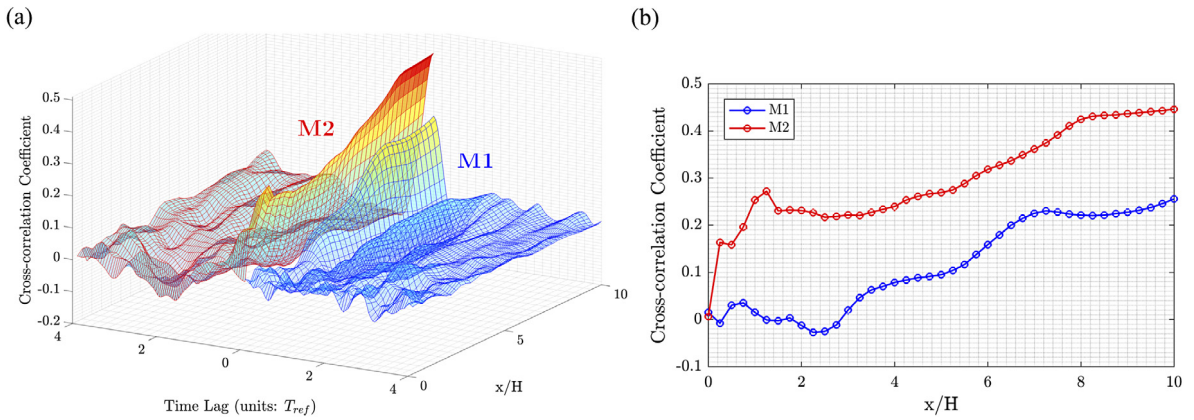

Fig. 12. The cross-correlation of V_{GF} at point pairs (presented as "∘" in Fig. 11) for investigating the wake's spanwise oscillation: (a): the cross-correlation profiles per pair; (b): a comparison of the cross-correlation coefficient at zero time lag.

This hypothesis is further studied by analysing the characteristics of the shedding from the bogies in the near and intermediate wake, and investigating the correlation in between. The characteristics of the spanwise shedding at the bogies, near and intermediate wake are represented by the V_{GF} at three typical points whose the locations ([x-coordinate, y-coordinate]) are highlighted by the triangle ("△"), cross ("+") and asterisk ("∗"), with the coordinates ($[-0.825H, -0.5W]$), ($[1H, -0.1667W]$) and ($[6H, -0.1667\ W]$) respectively, as shown in Fig. 11. Firstly, the frequency response at each point is presented in Fig. 13(a).

Fig. 13(a) illustrates that no dominant shedding frequency can be identified from the bogies. Instead a broad spectral response between $St_W = 0.2{\sim}2$ is identified within the near-wake region, which is likely due to the various length scales introduced by the bogies generating a range of different frequencies. In the intermediate-wake region, where the short length-scale turbulence structures are dissipated and the coherent counter-rotating vortices are fully established, a clear peak frequency at $St_W = 0.6$ results. Additionally, this dominant frequency is identical to the one in M1, again which suggests that the frequency of the spanwise motion is a characteristic of the pair of counter-rotating vortices due to an inherent instability, regardless of the presence of the bogies. This hypothesis is further supported by the fact that an identical train model demonstrates a same spanwise oscillation frequency with different ground boundary conditions (Wang et al., 2018). Furthermore, the correlations between the points located near the bogie, and the near and intermediate wake are plotted in Fig. 13(b). The strong correlation between the near and intermediate wake points with a time-lag, which approximately equals to the wake advection time between the two points, implies that it is an identical flow feature that

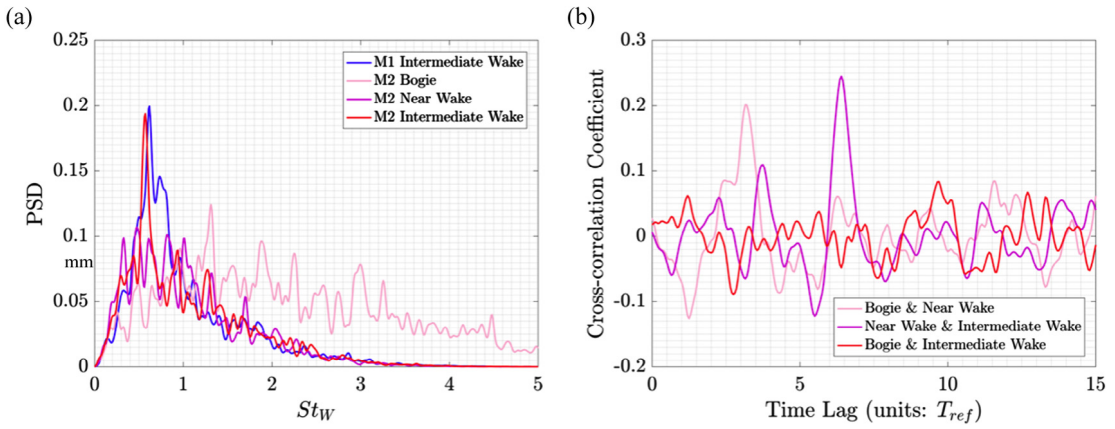

Fig. 13. The characteristics of the shedding from the bogies and spanwise wake oscillation, and the correlation between per two flow features based on V_{GF}: (a) the frequency response; (b) the cross-correlation between flow features.

convects downstream. Even though the shedding from the bogies is correlated to the near wake over a wide time-lag, it is not correlated with the intermediate wake. Therefore, instead of directly introducing the coherent spanwise oscillation at a particular frequency, the bogies demonstrate a global influence on the near-wake flow field through perturbing the flow over a wide frequency range. Additionally, our analysis suggests that the effects introduced by the bogies and the way that local flow disturbances interacts with the wake is general, although some variation may exist with different bogie configurations. The main reason for this view is that the shedding of flow structures introduced by the bogies shows no dominant frequency, but rather a broad frequency spectrum, and this frequency content is only locally correlated with the near wake region, while further downstream the wake propagation region is dominated by a spanwise oscillation with a frequency that does not match.

3.2. Slipstream assessment

In this section, the slipstream velocity is studied from two perspectives: based on (1) statistical slipstream profiles and (2) gust analysis. The statistical slipstream profiles illustrate the time-average and standard derivation of the slipstream velocity at the TSI specified assessment locations, and hereby, derive the maximum slipstream velocity ($U_{slipstream,max}$) based on a 95% confidence interval assuming Normally distributed statistics. Gust analysis tries to artificially replicate the field measurements of full-scale testing to obtain an ensemble average of the temporal slipstream data under TSI specifications (European Union Agency for Railways, 2014).

3.2.1. Statistical slipstream profiles

In this study, the statistical slipstream assessment is taken at the TSI specified trackside height ($z = 0.05H$) and platform height ($z = 0.35H$), over the streamwise range $x = -15H{\sim}30H$. The time-averaged and standard deviation profiles of the slipstream velocity ($U_{slipstream}$), and their streamwise (U_{GF}) and spanwise (V_{GF}) velocity components at the two measurement heights are plotted in Fig. 14, and critical points are listed in Table 3. Also plotted in this figure are experimental wind-tunnel measurements and numerical predictions from Wang et al. (2018) for a setup with a stationary ground with stationary wheels for comparison. This is partially to provide confidence in the numerical model, noting that the numerical predictions are close to the experimental results, with upstream deviations most likely due to background wind-tunnel turbulence, and also to provide a point of comparison to a case with a stationary ground/stationary wheel setup as is often necessarily the case for wind-tunnel testing. Further details concerning the comparison of experimental measurements and numerical predictions for this related case are provided in Wang et al. (2018). The maximum expected slipstream velocity ($U_{slipstream,max}$), which is defined as $\overline{U}_{slipstream} + 2\sigma_{slipstream}$, predicts the upper limit of slipstream velocity under 95% confidence interval assuming Normally distributed samples. As illustrated in Fig. 14, the bogies alter the slipstream profiles in the same manner, but their influence is more significant at the trackside height; thus, the discussion of the bogie effects on slipstream profiles focuses on the influence at the trackside height.

Over the train and in the near wake, it can be seen that M1 and M2 have qualitatively near identical $\overline{U}_{slipstream}$ profiles, which include the head pulse and a local peak around the tail. After the air passes over the tail, it accelerates and to achieve a maximum velocity before gradually decreasing. This is a typical HST slipstream profile, which has been identified for different train geometries with various techniques (Bell et al., 2016a; Huang et al., 2016; Baker, 2010; Bell et al., 2015). Quantitatively, the time-averaged velocity ($\overline{U}_{GF}$, $\overline{V}_{GF}$) profiles prior to the tail region are identical, except for local fluctuations caused by the bogies captured for M2.

Table 3
The critical values in the statistical slipstream profile analysis.

	M1		M2	
	Maximum	Location (x/H)	Maximum	Location (x/H)
	Trackside height ($\mathbf{z = 0.05H}$)			
$\overline{U}_{slipstream}$	0.076	−12.63	0.078	−12.63
$\sigma_{slipstream}$	0.028	14.28	0.063	5.61
$U_{slipstream,max}$	0.096	20.01	0.190	6.61
	Platform height ($\mathbf{z = 0.35H}$)			
$\overline{U}_{slipstream}$	0.087	−12.57	0.089	−12.57
$\sigma_{slipstream}$	0.015	24.79	0.0263	18.06
$U_{slipstream,max}$	0.087	−12.57	0.089	−12.57

Within region around the tail ($x = -1H \sim 1H$), both models show peaks in $\overline{U}_{GF}$ and $\overline{V}_{GF}$, with the flat underbody amplifying the magnitude of this disturbance. Hence, M1 demonstrates a higher local peak of $\overline{U}_{slipstream}$ around the tail. The reason for this difference is that with a smoother train surface, the flow over the tail is more streamlined and results in a higher magnitude effect at the measurement locations.

The figure also shows that $\overline{U}_{slipstream}$ initially drops in wake region before recovering further downstream. For M1, after the flow passes the tail, $\overline{U}_{slipstream}$ drops to approximately 0.005 at $x = 3H$, and then slowly increases to reach a maximum of 0.04 at $x = 25H$. In contrast, M2 shows a much steeper increase of $\overline{U}_{slipstream}$ starting from $x = 2H$, and achieves its maximum of 0.07 at $x = 7H$. According to $\overline{U}_{GF}$ and $\overline{V}_{GF}$, it can be seen that, the difference in $\overline{U}_{slipstream}$ between M1 and M2 is caused by the change to $\overline{U}_{GF}$. The underlying mechanism is that a sideways shift of the vortical wake structures, which contain lower momentum fluid, can significantly affect the local slipstream velocity. Details of time-mean wake structure were presented in Section 3.1.

In M2, both $\sigma_{U_{GF}}$ and $\sigma_{V_{GF}}$ show a gradual increase along the train due to the unsteadiness introduced by the bogies, while for M1 the standard deviations are negligible. Additionally, the perturbation caused by the bogies significantly intensifies $\sigma_{slipstream}$ within the wake region, which results in an increase of maximum $\sigma_{slipstream}$ from 0.028 to 0.063. According to the combined effects of $\overline{U}_{slipstream}$ and $\sigma_{slipstream}$, $U_{slipstream,max}$ is predicted to occur at $20H$ and $7H$ with the magnitude of 0.1 and 0.19, respectively, for M1 and M2. Therefore, although the head pulse causes a maximum $\overline{U}_{slipstream}$, the wake region is more critical in terms of maximum potential slipstream velocity due to the high turbulence level within the wake region, leading to considerable excursion from the mean behaviour.

3.2.2. Gust analysis

The TSI regulations (European Union Agency for Railways, 2014) define how the slipstream velocity should be measured under field testing, and the procedure of calculating the maximum slipstream velocity (also known as the *TSI value*) is briefly described here. The slipstream should be measured at two fixed positions: the trackside ($z = 0.05H$) and platform ($z = 0.35H$) height, as introduced before. The entire flow disturbance, including the train passing and the wake, needs to be recorded. Additionally, a *1-s Moving Average (1 s MA) filter* is required to be applied to the raw data, and the peak slipstream velocity of the filtered data is taken as one measurement. The distance between two independent measurements has to be more than 20 m, and a minimum of 20 independent measurements is required for calculating the maximum slipstream velocity (the *TSI value*). The *TSI value* is calculated as the mean of the peak velocities plus two standard deviations, which indicates the statistical maximum slipstream velocity of the HST within a 95% confidence level, and this assessment is integrated into the HST acceptance procedure.

Numerically, *Gust Analysis* tries to artificially replicate the field measurements of full-scale testing to obtain an ensemble average of the temporal slipstream data based on the above procedure. This study utilises the *Moving Probe Technique* to conduct the gust analysis, and the results are presented in Fig. 15. This technique was initially proposed by Muld et al. (2012b) to study slipstream, and was adopted by Wang et al. (2017, 2018) to investigate the performance of turbulence models on HST slipstream prediction and the effect of the ground boundary condition on HST slipstream. A full description of the *Moving Probe technique* can be found in Wang et al. (2017, 2018).

The $U_{slipstream}$ disturbance recorded by each probe is plotted as a function of time as a light grey line, and the peak value of each measurement is highlighted by a black dot. The results with a 1s MA filter are plotted as blue lines, for which the peak values are highlighted by blue points. Similar to the full-scale testing (Baker et al., 2014) and moving-model experiments (Bell et al., 2015), gust analysis shows a large run-to-run variance. Consistent with the statistical results presented in Section 3.2.1, the difference is more significant at the lower height ($z = 0.05H$). In M2, a shape increase of $U_{slipstream}$ after the tail passage is identified, and the peak slipstream velocities (U_{peak}) within the wake region demonstrate a strong left-skewness. In contrast, M1 shows that peak slipstream velocities have a lower magnitude and their occurrence is significantly delayed downstream. This difference is due to the wider and more turbulent wake structure caused by the bogies, which is discussed and presented in Section 3.1. As presented in Table 4, the *TSI value* assessment is sensitive to the presence of the bogies, especially at a lower height. Table 4 determines that the effect of bogies on the wake structures can significantly vary the slipstream assessment, i.e. the presence of bogies can alter the *TSI value* up to 20% at the trackside height.

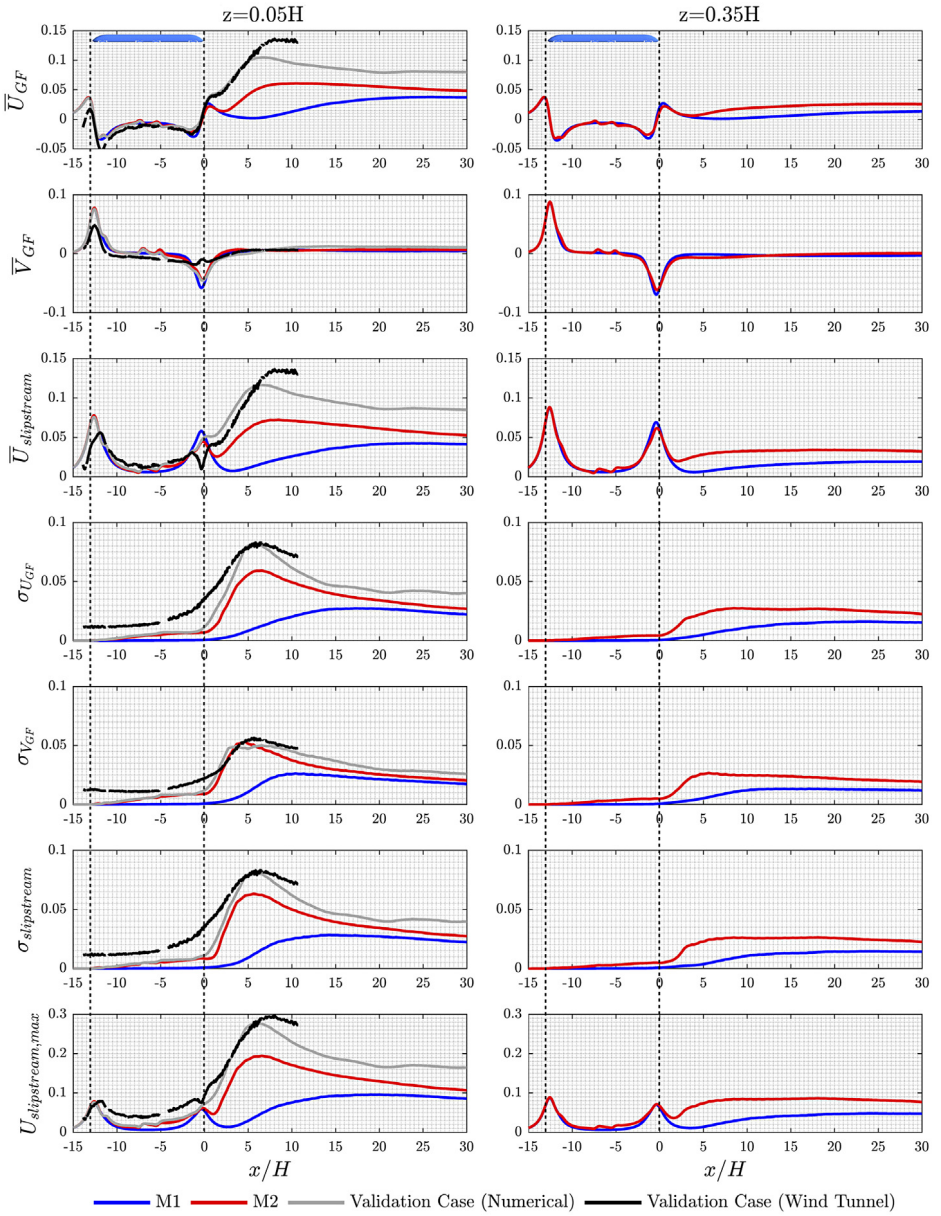

Fig. 14. The comparison of statistical slipstream profiles between M1 and M2 at trackside ($z = 0.05H$) (left column) and platform ($z = 0.35H$) (right column) heights. The wind-tunnel measurements (Bell et al., 2017) and associated numerical validation (Wang et al., 2017) added to the figures in the left column are for a different setup of a stationary ground with stationary wheels. These are provided for validation and reference.

Table 4
The critical values from the gust analysis. The numbers in the brackets are the raw data before applying a 1 s moving average.

		Trackside	Platform
M1	$\overline{U}_{peak}$	0.050 (0.090)	0.031 (0.088)
	$\sigma_{U_{peak}}$	0.021 (0.018)	0.009 (0.002)
	$U_{TSI,max}$	0.092 (0.126)	0.049 (0.091)
M2	$\overline{U}_{peak}$	0.079 (0.175)	0.045 (0.100)
	$\sigma_{U_{peak}}$	0.018 (0.065)	0.013 (0.023)
	$U_{TSI,max}$	0.114 (0.303)	0.072 (0.145)

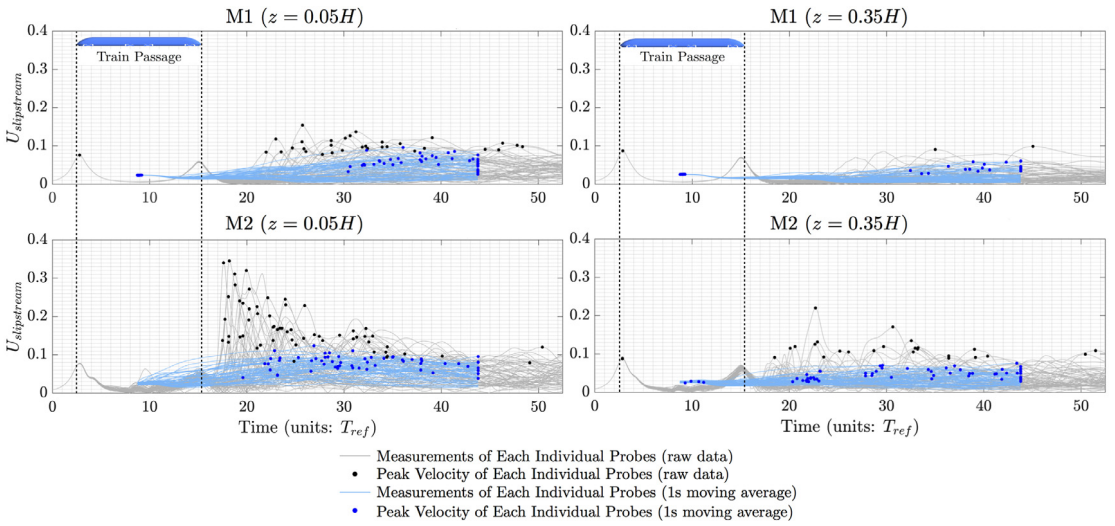

Fig. 15. The results of gust analysis based on the *Moving Probe Technique* under TSI specifications.

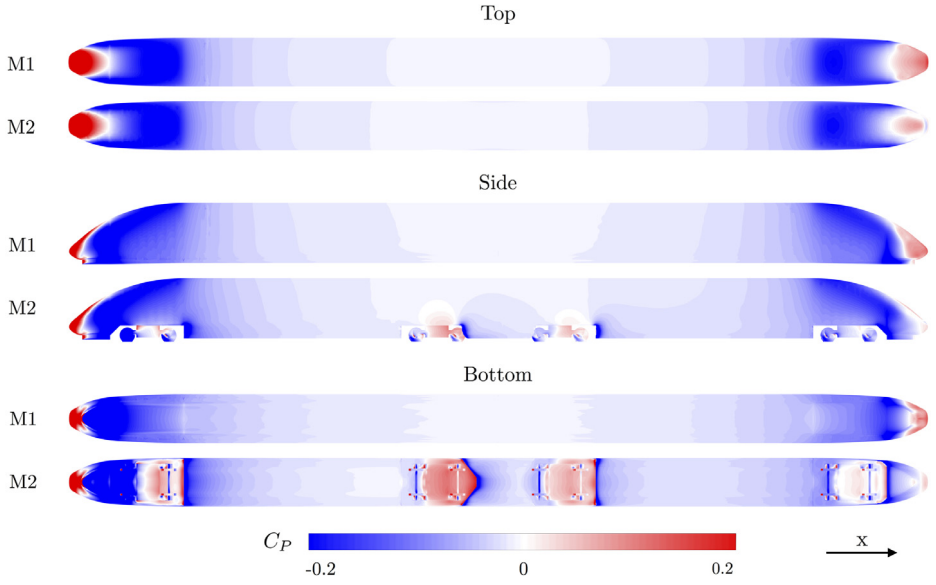

Fig. 16. The comparison of the aerodynamic loading on the train surface based on the pressure coefficient (C_P).

3.3. Aerodynamic loading

In the final section, the bogie effect on the aerodynamic loading is presented according to the changes induced on the train surface pressure and force integral. The surface pressure is visualised by the pressure coefficient (C_P) as presented in Fig. 16, where C_P is defined by

$$C_P = \frac{P - P_\infty}{\frac{1}{2}\rho_\infty V_\infty^2}. \tag{3}$$

Here, P is the surface static pressure, and reference values for the pressure, density and velocity are P_∞, ρ_∞ and V_∞, respectively. Fig. 16 shows that the top and side surface pressure distributions are qualitatively identical, and a more quantitatively comparison is obtained by the pressure profiles on the train centreplane surfaces in Fig. 17.

A high pressure region due to the impact of the oncoming flow is captured at the head, and the negative pressure region along the curved surface is caused by local flow acceleration. Additionally, a positive pressure region can be identified for both models at the tail due to the reversed flow, while the area of this region for M2 is reduced towards the lower height due

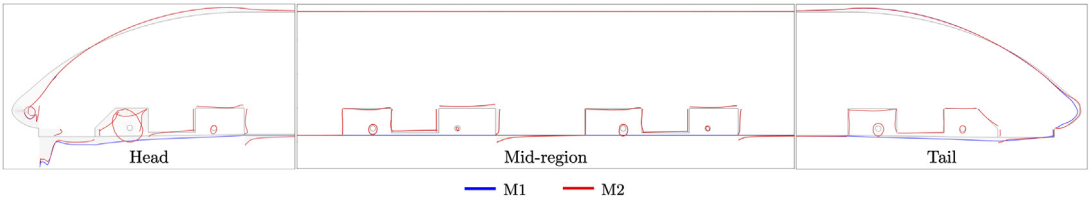

Fig. 17. The centreplane pressure profiles at each train section for a quantitative comparison of the bogie effects on the aerodynamic loading.

Table 5
The comparison of the drag (C_D) and lift (C_L) estimation between M1 and M2.

		M1	M2
C_D	**Mean**	0.157	0.283
	Standard deviation	9.11×10^{-4}	9×10^{-3}
C_L	**Mean**	−0.078	0.051
	Standard deviation	0.0039	0.016

to the alteration to the flow caused by the bogies. Clearly, the major differences occur over the bottom surface. Comparing the streamlined M1 bottom surface, the bogies not only increase drag through the introduction of blockage, the cavity flow within the bogie cut-outs also produce a positive pressure on the bottom surface, which affects the lift force. From the C_P distribution over the train surface, both the drag (C_D) and lift (C_L) coefficients are calculated and listed in Table 5. Not surprisingly, due to the altered surface pressure, the presence of the bogies can alter C_D by almost a factor of 2 (from $C_D = 0.157$ to 0.283). This is consistent with the results of a previous study concluding that bogies are a major aerodynamic drag source, even though the train length-to-height ratio in this study is reduced (Raghunathan et al., 2002). The formation of positive pressure regions on the bottom surface alters C_L from a negative value of −0.078 to a positive value of 0.051. Additionally, the local flow shedding introduced by the bogies amplifies the unsteadiness of the aerodynamic loading on the train and results in a significant increases of the standard deviations of C_D and C_L, as shown in Table 5.

3.4. Summary of key findings

In this study, the effects of bogies on HST slipstream characteristics are investigated based on two generic train models: a *Simplified Train Model* (M1) without the bogies, and *Full-featured Train Model* (M2) with the simplified bogies. Through a direct comparison of the time-mean and instantaneous flow structures between M1 and M2, the mechanism of how the bogies alter the slipstream characteristics around the train is elucidated. The origin of the altered flow is that the bogies partially block the underbody flow stream and increase its unsteadiness due to the significant introduced flow perturbations. Without the bogies, a high momentum flow stream from underneath forms a time-mean secondary vortex pair (vortex pair B) around the snowplough, which is not identified in the M2 model. This vortex pair is about 32.1% weaker than the primary downwash pillar vortices (vortex pair A). Additionally, no significant correlation is determined between oscillations of the vortices from each side; instead, a strong correlation between trailing vortices from the two vortex pairs on the same side is identified indicating a near-wake vertical energy oscillation. Without the presence of vortex pair B, the downwash flow from the top of the tail in M1 forms a pair of counter-rotating vortices (vortex pair C), immediately behind the tail, and establishes a spanwise oscillation. The pillar vortices in the near wake ($x/H = 0.5$) for both M1 and M2 show similar identifiable peak frequencies of $St_W = 0.75$ and 0.6 based on the pressure signal, while vortex pair B for M1 shows a wider spectrum with no clearly identifiable dominant frequency. As the flow advects downstream, the vortex pairs A and B of M1 merge into a single coherent vortex pair (vortex pair C), similar to the case for M2. The strength of each vortex of C for M2 is 30% greater than that for M1, while the bogies cause a higher wake decay rate due to the unsteadiness introduced into the wake.

The appearance of a spanwise wake oscillation is found to be correlated with the presence of counter-rotating vortices of vortex pair C, instead of the presence of bogies, according to the following observations. Firstly, the spanwise oscillation has an similar frequency of approximately $St_W \simeq 0.6$ based on spanwise velocity, regardless of the presence or absence of bogies. Secondly, the delay in the establishment of the spanwise wake oscillation is consistent with the longer wake formation region of M1, until vortex C forms. Furthermore, the shedding/turbulent flow from the bogies shows a wide frequency spectrum, which feeds into the near-wake. Therefore, this study proposes that the spanwise motion is not directly triggered by shedding from the bogies; instead, the wide spectrum turbulence generated perturbs the forming counter-rotating vortex pair (vortex pair C) which responds at a preferred convective instability frequency as a spanwise oscillation. Even though the bogies do not directly generate the spanwise motion, they may affect the spanwise oscillation by altering the near wake turbulence level, which deposits energy into the intrinsic instability mode, and also the altering strength of the counter-rotating vortices. In terms of this analysis, it needs to be pointed out that the train geometry used for this study consists of only two carriages,

so it is much shorter than typical high-speed trains. It is possible that the increased number of bogies of longer trains may have a stronger influence on downstream wake development than is seen here.

As the wake convects downstream, the pair of counter-rotating vortices moves apart from each other in the spanwise direction. In M2, the strength of the trailing vortices is stronger and they are closer to the slipstream assessment location. Because of this, $\overline{U}_{slipstream}$ is increased due to the increment of $\overline{U}_{GF}$, especially within the wake region. Additionally, the unsteadiness introduced by the bogies increases the standard deviation of velocity components, and result in a significantly greater prediction of $U_{slipstream,max}$. Even though this effect occurs at both slipstream assessment heights, the impact is more significant at the trackside height of $x = 0.05H$ than the platform height of $x = 0.35H$. Similar influences are determined based on the gust analysis, which shows that the *TSI value* at the trackside height is increased from 0.092 to the 0.114 due to the presence of bogies. The bogies also alter the train surface pressure distribution especially on the bottom surface, which results in a significant increase in C_D from 0.157 to 0.283, and a change in C_L from -0.078 to 0.051. The unsteadiness caused by the bogies is also reflected in increases of the standard deviations of the aerodynamic loadings.

4. Conclusion

In conclusion, the mechanism of how bogies alter the slipstream characteristics is uncovered by analysing the effects on the wake structures including the time-averaged flow features, and their dynamic responses at each stage of the flow development. This study shows that by altering the underbody flow condition, the bogies predominantly change the wake formation topology by generating a pair of recirculation zones under the train tail region. Dynamically, the bogies significantly increase both the underbody flow and wake's turbulence level due to the unsteadiness from induced flow perturbations. This study determines the inter-relationship between the bogies and spanwise wake oscillation. Specifically, by showing that the spanwise motion of the wake occurs without the presence of the bogies at the same oscillation frequency, this study argues that the bogies do not directly cause this oscillation; instead, the present study proposes that the spanwise motion is due to a natural convective instability of the trailing vortex pair. The presence of the bogies merely generates the turbulence that leads to the early detection of the oscillation as it is amplified downstream. Both statistical and gust analyses show that the alteration of wake flow structures due to the bogies can further increase slipstream, especially at a lower reference height. Additionally, the variation of the train surface pressure due to the bogies can significantly alter the prediction of aerodynamic loading. Above all, this study has provided insight into bogie effects on HST slipstream characteristics by systematically comparing the flow features between train models with and without bogies.

References

Baker, C., 2010. The flow around high speed trains. J. Wind Eng. Ind. Aerodyn. 98 (6), 277–298.

Baker, C.J., Quinn, A., Sima, M., Hoefener, L., Licciardello, R., 2014. Full-scale measurement and analysis of train slipstreams and wakes. Part 2 Gust analysis. Proc. Inst. Mech. Eng. F 228 (5), 468–480.

Bell, J., Burton, D., Thompson, M., Herbst, A., Sheridan, J., 2015. Moving model analysis of the slipstream and wake of a high-speed train. J. Wind Eng. Ind. Aerodyn. 136, 127–137.

Bell, J., Burton, D., Thompson, M., Herbst, A., Sheridan, J., 2016a. Flow topology and unsteady features of the wake of a generic high-speed train. J. Fluids Struct. 61, 168–183.

Bell, J., Burton, D., Thompson, M., Herbst, A., Sheridan, J., 2016b. Dynamics of trailing vortices in the wake of a generic high-speed train. J. Fluids Struct. 65, 238–256.

Bell, J., Burton, D., Thompson, M., Herbst, A., Sheridan, J., 2017. A wind-tunnel methodology for assessing the slipstream of high-speed trains. J. Wind Eng. Ind. Aerodyn. 166, 1–19.

Cooper, R., 1981. The effect of cross-winds on trains. J. Fluids Eng. 103, 170–178.

Copley, J., 1987. The three-dimensional flow around railway trains. J. Wind Eng. Ind. Aerodyn. 26 (1), 21–52.

DIN Standards Committee Railway/Normenausschuss Fahrweg und Schienenfahrzeuge (FSF), 2018.

European Committee for Standardization (CEN), 2009. Railway applications — aerodynamics part 4: Requirements and test procedures for aerodynamics on open track, CEN EN 14067-4.

European Union Agency for Railways, 2014. Commission Regulation (EU) No 1302/2014 concerning a technical specification for interoperability relating to the 'rolling stock — locomotives and passenger rolling stock' subsystem of the rail system. Off. J. Eur. Union.

Fluent, I., 2006. FLUENT 6.3 user's guide. Fluent documentation.

García, J., Crespo, A., Berasarte, A., Goikoetxea, J., 2011. Study of the flow between the train underbody and the ballast track. J. Wind Eng. Ind. Aerodyn. 99 (10), 1089–1098.

Graftieaux, L., Michard, M., Grosjean, N., 2001. Combining PIV, POD and vortex identification algorithms for the study of unsteady turbulent swirling flows. Meas. Sci. Technol. 12 (9), 1422.

Huang, S., Hemida, H., Yang, M., 2016. Numerical calculation of the slipstream generated by a CRH2 high-speed train. Proc. Inst. Mech. Eng. F 230 (1), 103–116.

Jönsson, M., Wagner, C., Loose, S., 2014. Particle image velocimetry of the underfloor flow for generic high-speed train models in a water towing tank. Proc. Inst. Mech. Eng. F 228 (2), 194–209.

Kaltenbach, H.-J., Portillo, I.A., Schober, M., 2008. A generic train-underfloor experiment for CFD validation. In: BBAA VI International Colloquium on: Bluff bodies aerodynamics and applications. Citeseer, pp. 20–24.

Mancini, G., Malfatti, A., Violi, A.G., Matschke, G., 2001. Effects of experimental bogie fairings on the aerodynamic drag of the ETR 500 high speed train. In: Proceedings of the World Congress of Railway Research WCRR.

Muld, T.W., Efraimsson, G., Henningson, D.S., 2012a. Flow structures around a high-speed train extracted using proper orthogonal decomposition and dynamic mode decomposition. Comput. & Fluids 57, 87–97.

Muld, T.W., Efraimsson, G., Henningson, D.S., 2012b. Mode decomposition and slipstream velocities in the wake of two high-speed trains. Int. J. Rail. Technol..

Östh, J., Kaiser, E., Krajnović, S., Noack, B.R., 2015. Cluster-based reduced-order modelling of the flow in the wake of a high speed train. J. Wind Eng. Ind. Aerodyn. 145, 327–338.

Pereira, I., André, J.M.C., 2013. A semi-analytical model of the 3D boundary layer over the streamlined nose of a train. J. Wind Eng. Ind. Aerodyn. 119, 78–88.
Pii, L., Vanoli, E., Polidoro, F., Gautier, S., Tabbal, A., 2014. A full scale simulation of a high speed train for slipstream prediction. In: Transport Research Arena (TRA) 5th Conference: Transport Solutions from Research to Deployment.
Quinn, A., Hayward, M., Baker, C., Schmid, F., Priest, J., Powrie, W., 2010. A full-scale experimental and modelling study of ballast flight under high-speed trains. Proc. Inst. Mech. Eng. F 224 (2), 61–74.
Raghunathan, R.S., Kim, H.-D., Setoguchi, T., 2002. Aerodynamics of high-speed railway train. Progr. Aerosp. Sci. 38 (6), 469–514.
Sima, M., Gurr, A., Orellano, A., 2008. Validation of CFD for the flow under a train with 1: 7 scale wind tunnel measurements. In: Proceedings of the BBAA VI International Colloquium on Bluff Bodies Aerodynamics and Applications, Milano, Italy.
Sirovich, L., 1987. Turbulence and the dynamics of coherent structures part I: coherent structures. Q. Appl. Math. 45 (3), 561–571.
Soper, D., Flynn, D., Baker, C., Jackson, A., Hemida, H., 2017. A comparative study of methods to simulate aerodynamic flow beneath a high-speed train. Proc. Inst. Mech. Eng. F 0954409717734090.
Spalart, P.R., 2009. Detached-eddy simulation. Ann. Rev. Fluid Mech. 41, 181–202.
Wang, S., Bell, J.R., Burton, D., Herbst, A.H., Sheridan, J., Thompson, M.C., 2017. The performance of different turbulence models (URANS, SAS and DES) for predicting high-speed train slipstream. J. Wind Eng. Ind. Aerodyn. 165, 46–57.
Wang, S., Burton, D., Herbst, A.H., Sheridan, J., Thompson, M.C., 2018. The effect of the ground condition on high-speed train slipstream. J. Wind Eng. Ind. Aerodyn. 172, 230–243.
Yao, S.-B., Sun, Z.-X., Guo, D.-L., Chen, D.-W., Yang, G.-W., 2013. Numerical study on wake characteristics of high-speed trains. Acta Mech. Sinica 29 (6), 811–822.
Zhang, J., Li, J.-j., Tian, H.-q., Gao, G.-j., Sheridan, J., 2016. Impact of ground and wheel boundary conditions on numerical simulation of the high-speed train aerodynamic performance. J. Fluids Struct. 61, 249–261.